

Kondo screening cloud in the single-impurity Anderson model: A density matrix renormalization group study

Andreas Holzner,^{1,2} Ian P. McCulloch,³ Ulrich Schollwöck,¹ Jan von Delft,^{1,4} and Fabian Heidrich-Meisner^{2,4}

¹*Physics Department, Arnold Sommerfeld Center for Theoretical Physics, and Center for NanoScience, Ludwig-Maximilians-Universität München, D-80333 München, Germany*

²*Institute for Theoretical Physics C, RWTH Aachen University, D-52056 Aachen, Germany*

³*School of Physical Sciences, University of Queensland, Brisbane, Queensland 4072, Australia*

⁴*Kavli Institute for Theoretical Physics, Kohn Hall, University of California, Santa Barbara, California 93106, USA*

(Received 19 June 2009; published 13 November 2009)

A magnetic moment in a metal or in a quantum dot is, at low temperatures, screened by the conduction electrons through the mechanism of the Kondo effect. This gives rise to spin-spin correlations between the magnetic moment and the conduction electrons, which can have a substantial spatial extension. We study this phenomenon, the so-called Kondo cloud, by means of the density matrix renormalization group method for the case of the single-impurity Anderson model. We focus on the question whether the Kondo screening length, typically assumed to be proportional to the inverse Kondo temperature, can be extracted from the spin-spin correlations. For several mechanisms—the gate potential and a magnetic field—which destroy the Kondo effect, we investigate the behavior of the screening cloud induced by these perturbations.

DOI: [10.1103/PhysRevB.80.205114](https://doi.org/10.1103/PhysRevB.80.205114)

PACS number(s): 78.20.Bh, 02.70.-c, 72.15.Qm, 75.20.Hr

I. INTRODUCTION

The Kondo effect,¹ a well-known feature of magnetic impurity systems, has seen a tremendous renewed interest due to the realization of quantum dots and nanoscale systems.² The existence of Kondo correlations at low temperatures T has been firmly established in numerous experiments on quantum dots,³ molecules,⁴ and carbon nanotubes.⁵ The interaction of an impurity spin with itinerant electrons, causing the Kondo effect, manifests itself in spatially extended spin-spin correlations—the Kondo screening cloud. These correlations have been extensively studied in theory^{6–15} and many proposals for experimentally measuring the Kondo screening cloud have been put forward.^{9,11,14,15} Also, several studies have emphasized the emergence of mesoscopic fluctuations on finite systems, and the existence of even-odd effects in the Kondo cloud when computed from a lattice model.^{8,9,11,16,17} While there has been experimental progress toward the measurement of the Kondo cloud,^{18,19} the detection of the spin-spin correlations has proven to be highly challenging and has not been accomplished so far. Depending on the Kondo temperature T_K , the Kondo cloud can have a significant extension of $\sim 1 \mu\text{m}$.¹³

In our work, we examine the spin-spin correlations in a real-space model, the single-impurity Anderson model (SIAM) that includes charge fluctuations, using the density matrix renormalization group method (DMRG).^{20–22} We address two main questions: first, we compute the spin-spin correlations between the impurity spin and the conduction electrons at particle-hole symmetry and discuss how the Kondo screening length ξ_K can be directly extracted from such data. To that end, we discuss several ways of collapsing spin-spin correlations calculated for different Kondo temperatures onto a universal curve. In this analysis, we employ ideas suggested by Gubernatis *et al.*⁶ that have also been used in previous DMRG studies of the Kondo cloud problem.^{11,12} We find that from chains of about $L=500$ sites,

suitable measures for the $L=\infty$ screening length can be extracted for Kondo temperatures of $k_B T_K / \Gamma \sim 1 \cdot 10^{-3}$ (Γ is the tunneling rate). Knowledge of the universal curve further allows us to estimate ξ_K even for Kondo temperatures for which the accessible system sizes are too small to host the full Kondo cloud. As a main result of our analysis, we find that our measures of ξ_K extracted from the spin-spin correlations have the same functional dependence on model parameters as ξ_K^0

$$\xi_K^0 = \hbar v_F / T_K, \quad (1)$$

at particle-hole symmetry (v_F is the Fermi velocity in the leads, we adopt $k_B=1$ throughout the rest of this work). The screening length ξ_K^0 governs the finite-size scaling of local quantities such as the polarization or the magnetic moment.⁸

Second, we consider several mechanisms that destroy Kondo correlations, namely, a gate voltage and a magnetic field applied to the quantum dot. We study the changes in the screening length induced by a variation in these parameters. We argue that computing the magnetic-field dependence of the screening length provides a means of extracting the Kondo temperature.

The emergence of an exponentially small energy scale in the Kondo problem, namely, T_K , restricts any real-space approach with respect to the Kondo temperatures that can be accessed. A powerful framework was introduced by Wilson²³ in the form of the numerical renormalization group (NRG) method,^{23,24} which is explicitly tailored toward the Kondo problem. This is achieved through the introduction of a logarithmic energy discretization that allows the Kondo scale to be resolved but loses real-space information. Recently, an NRG method has been developed to access spatially resolved quantities,^{13,14,25} extending some older NRG calculations for spatially dependent correlation functions.²⁶ Using the more recent NRG approach,¹³ the spin correlations between the impurity and the sites in the leads have been computed for

the Kondo model, and it has been shown that at the Kondo screening length ξ_K^0 , the envelope of the correlations crosses over from a $1/x$ decay at distances $x < \xi_K^0$ to a $1/x^2$ decay at distances $x > \xi_K^0$, where x denotes the distance between the impurity and a site in the leads.

Comparing NRG and DMRG, first, there are technical differences between DMRG and NRG with respect to how the spin-spin correlations $\langle \vec{S}_i \cdot \vec{S}_j \rangle$ (\vec{S}_i denotes a spin-1/2 operator at site i) are obtained. NRG requires a separate run for each pair of indices, (i, j) , whereas DMRG operates directly on real-space leads. That way, after calculating the ground state for a system of a given length, all correlations can be evaluated in a single run. While the use of real-space chains is restricted to one dimension, which is the case of interest in our work, NRG in principle works for higher dimensions too. Second, using DMRG, we can gain direct and easy information on the finite-size scaling of spin-spin correlations, which we heavily exploit in our analysis. Most importantly, DMRG can also be applied to quantum-impurity problems with interacting leads¹² that NRG is not designed for.

DMRG has previously been used to study the Kondo cloud in several papers, for both the single-impurity Anderson model¹¹ and the Kondo model.^{8,10} In Ref. 11 by Hand *et al.*, in particular, an interesting relation between the screening length as extracted from the spin correlations and the weight of the Kondo resonance has been discussed. Our study extends the DMRG literature as we consider the mixed-valence regime, the effect of a magnetic field, and we discuss and demonstrate the universal scaling of spin-spin correlations for a wide range of parameters. Moreover, in the absence of a magnetic field, we exploit the SU(2) symmetry of the model in the spin sector in the DMRG simulations, which we find is crucial for efficiently obtaining reliable numerical results.

Besides the conceptual interest in understanding the scaling properties of the Kondo screening length with both system size and Kondo temperature, our results are relevant to gauge the range of validity of numerical approaches for calculating the conductance of nanostructures that employ a real-space representation of the leads such as time-dependent DMRG simulations of transport in the single-impurity Anderson model.^{27–29} Moreover, the approaches discussed here to extract the screening length could be applicable to more complex geometries in a straightforward way, for instance, to multichannel and/or multidot problems.

Our work is organized as follows. In Sec. II, we introduce our model and define the quantities of interest. In Sec. III, the spin-spin correlations constituting the Kondo cloud are investigated and we demonstrate how to extract the value of the Kondo screening length ξ_K from the spin-correlation data, making use of the universal finite-size scaling behavior of ξ_K . We proceed with a discussion of the behavior of the screening length upon driving the system away from the Kondo point via a gate potential, presented in Sec. IV, and then turn to the case of a magnetic field in Sec. V. We conclude with a summary, Sec. VI, while technical detail on the method and computations are given in the Appendix.

II. MODEL

We model a quantum dot coupled to a lead by the single-impurity Anderson model, describing the lead by a tight-

binding noninteracting chain. This constitutes a one-channel problem

$$H = \sum_{\sigma=\uparrow,\downarrow} \epsilon_d n_{d\sigma} + BS_d^z + U n_{d\uparrow} n_{d\downarrow} - t \sum_{\sigma} \sum_{i=1}^{L-1} (c_{i\sigma}^\dagger c_{(i+1)\sigma} + \text{h.c.}) - \sum_{\sigma} \sqrt{2t'} (c_{1\sigma}^\dagger d_{\sigma} + \text{h.c.}). \quad (2)$$

$c_{i\sigma}$ annihilates an electron with spin $\sigma = \uparrow, \downarrow$ on site i , d_{σ} annihilates an electron with spin σ on the dot, and $n_{d\sigma} = d_{\sigma}^\dagger d_{\sigma}$. The spin operators at any site are given by $S_i^a = c_{i\sigma}^\dagger \sigma_{ss'}^a c_{i\sigma'}$, where σ^a are the Pauli matrices ($a = x, y, z$). ϵ_d denotes the gate potential and B denotes the magnetic field applied to the dot, U denotes the strength of the Coulomb interaction on the quantum dot, t' denotes the hopping of the dot levels to the first site in the lead, t denotes the hopping within the lead. The width of the dot level due to the hybridization with the lead is given by $\Gamma = 2t'^2/t$.

In the absence of a magnetic field, this model has a spin SU(2) symmetry. In our analysis, we calculate the ground state of this system via DMRG using an implementation³⁰ exploiting the SU(2) symmetry, which greatly improves the efficiency^{31,32} (see the Appendix for more detail). A typical run for $L=500$ sites with $m=1500$ states took about 60 h on a 2.6 GHz Opteron CPU.

All simulations, irrespective of ϵ_d , are performed at half-filling of the full system. As the Kondo scale depends exponentially on U/Γ , while in a real-space representation of the leads, the energy resolution is proportional to $1/L$, we restrict our analysis to the intermediate values of U/Γ . The trade-off for these limitations is that it is straightforward to calculate spin correlators, as outlined below [see Eq. (3)].

Throughout this work, we use chains with an overall *even* number of sites. It is well known that there are significant even-odd effects in impurity problem of this kind.^{8,9,11,16,17} Earlier work (see, e.g., Ref. 33), suggests that the convergence with system size toward a Kondo state is much faster on chains with an even number of sites. We thus work in singlet subspaces.

III. SPIN-SPIN CORRELATIONS AND KONDO SCREENING LENGTH AT $\epsilon_d = -U/2$

In this section, we present our results for the spin-spin-correlation function at particle-hole symmetry and we discuss two ways of collapsing the data, allowing for a determination of the Kondo screening length. In order to investigate the behavior of the Kondo screening length, we shall study the following integrated spin-correlation function

$$\Sigma(x) = 1 + \sum_{i=1}^x \frac{\langle \vec{S}_d \cdot \vec{S}_i \rangle}{\langle \vec{S}_d \cdot \vec{S}_d \rangle}, \quad (3)$$

to be evaluated in the singlet subspace of the total spin $\vec{S}_{\text{tot}} = \vec{S}_d + \sum_{i=1}^{L-1} \vec{S}_i$, and under the assumption that $\langle \vec{S}_d^2 \rangle \neq 0$ (x is given in units of the lattice constant). This definition is mo-

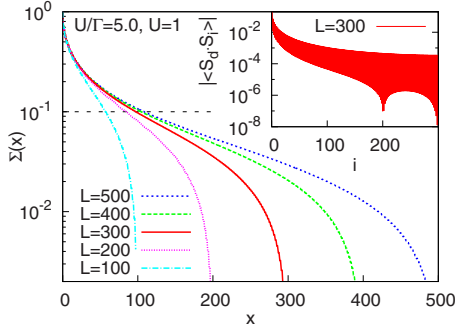
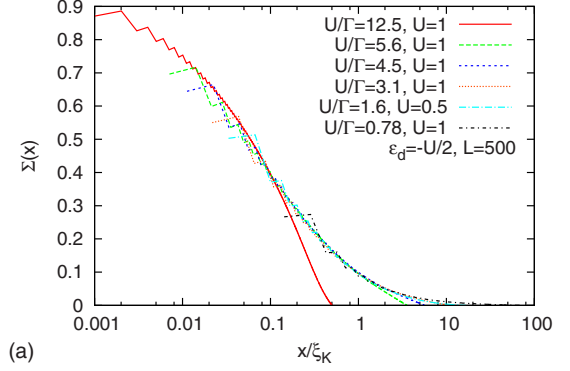


FIG. 1. (Color online) Integrated spin-spin correlations $\Sigma(x)$ [from Eq. (3)] for systems of different sizes at $U=1, \Gamma=0.20$ and $\epsilon_d=-U/2$. As an example, the threshold of 0.1 that we use in Eq. (5) to extract $\xi_{0,9}$ is indicated by the dashed horizontal line. As an illustration of the typical raw data, we show the absolute value of the spin-spin correlations $|\langle \vec{S}_d \cdot \vec{S}_i \rangle|$ for $L=300$ in the inset.

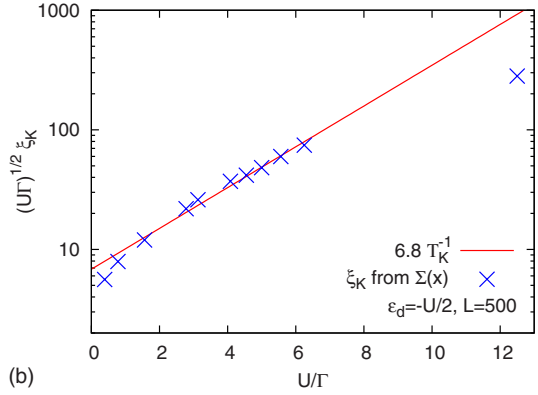
tivated by the following convenient properties: (i) the decay of $\Sigma(x)$ with x characterizes the extent to which the total spin of chain sites one to x is able to screen the spin on the impurity level, i.e., the extent to which $\sum_{i=1}^x \vec{S}_i$ has, crudely speaking, “become equal and opposite” to \vec{S}_d . (ii) When the sum includes the entire chain, we always have $\Sigma(L-1)=0$. This follows by noting that in the subspace with zero total spin, where $\langle \vec{S}_{\text{tot}}^2 \rangle = 0$, we have $\langle \vec{S}_d^2 \rangle = \langle (\sum_{i=1}^{L-1} \vec{S}_i)^2 \rangle$, and hence also $\langle \vec{S}_{\text{tot}}^2 \rangle = 2\langle \vec{S}_d \cdot \vec{S}_d \rangle \Sigma(L-1)$. (iii) The correlator is normalized to $\Sigma(0)=1$. (iv) In the absence of a magnetic field, $\Sigma(x)$ is SU(2) invariant, such that this symmetry can be exploited in our numerics. In the presence of a magnetic field, we shall use a symmetry-broken version, replacing $\langle \vec{S}_d \cdot \vec{S}_i \rangle / \langle \vec{S}_d \cdot \vec{S}_d \rangle$ by $(\langle S_d^x S_i^x \rangle - \langle S_d^y S_i^y \rangle) / (\langle S_d^x S_d^x \rangle - \langle S_d^y S_d^y \rangle)$.

As an example, the inset of Fig. 1 shows a DMRG result for the absolute value of the bare spin-spin correlator $\langle \vec{S}_d \cdot \vec{S}_i \rangle$. The feature at $i \sim 200$ is a simple effect of the open boundary conditions. The spin correlations for i smaller than a certain value (here roughly $i \sim 200$) oscillate between negative and positive, while beyond a certain point, all $\langle \vec{S}_d \cdot \vec{S}_i \rangle$ become positive. This feature at $i \sim 200$ precisely appears at the site where this happens, i.e., where $\langle \vec{S}_d \cdot \vec{S}_i \rangle$ with i even changes its sign and, as a consequence, the correlator passes arbitrarily close through zero. Summing up the correlator according to Eq. (3) yields $\Sigma(x)$, plotted in the main panel.

The notion of a screening length is based on the premise that the decay of $\Sigma(x)$ follows a universal form characterized by a single length scale, ξ_K , as long as this scale is significantly shorter than the system size, $\xi_K \ll L$. (According to the expectation that $\xi_K \propto \hbar v_F / T_K$, this condition is equivalent to the following statement: perfect spin screening in a system of finite size L can only be achieved if the level spacing, which scales like $\hbar v_F / L$, is smaller than T_K .) Whenever this condition is not met, the shape of the decay of $\Sigma(x)$ with x deviates from its universal form once x becomes large enough such that the finite system size makes itself felt [via the boundary condition $\Sigma(L-1)=0$]. To extract ξ_K from DMRG data obtained for finite-sized systems, we thus need a strategy for dealing with this complication. Below, we shall describe two different approaches that accomplish this, both involving a scaling analysis.



(a)



(b)

FIG. 2. (Color online) (a) Rescaled integrated spin-spin correlations $\Sigma(x)$, collapsed onto a universal curve via suitable choices of ξ_K . (b) Comparison of the U and Γ dependence of ξ_K and ξ_K^0 [from Eq. (4)]: $\sqrt{U\Gamma} \xi_K$ (symbols) and $\sqrt{U\Gamma} p T_K^{-1}$ (lines) plotted vs U/Γ , using p as the fitting parameter (resulting in $p=6.8$).

To check whether the screening length obtained using either of the two scaling strategies conforms to the theoretical expectations, we shall check whether its dependence on the parameters U , Γ , and ϵ_d agrees with that of the length scale $\xi_K^0 = \frac{\hbar v_F}{T_K}$ [Eq. (1)]. Using the known form of the Kondo temperature T_K for the Anderson model,^{34,35} this dependence is given by

$$\xi_K^0 \equiv \frac{\hbar v_F}{\sqrt{U\Gamma}} \exp \left[\frac{\pi |\epsilon_d| |\epsilon_d + U|}{2U\Gamma} \right]. \quad (4)$$

We shall indeed find a proportionality of the form $\xi_K = p \xi_K^0$, where the numerical prefactor p reflects the fact that the definition of T_K involves an arbitrary choice of a prefactor on the order of one. We emphasize, however, that our determination of ξ_K will be carried out without invoking Eq. (4); rather, our results for ξ_K will turn out to confirm Eq. (4) *a posteriori*. In the present section we shall focus on the symmetric Anderson model ($\epsilon_d = -U/2$) at zero magnetic field, considering more general cases in Sec. IV.

A. Scaling collapse of $\Sigma(x)$

The first way of extracting the screening length is to plot $\Sigma(x)$ versus x/ξ_K , where ξ_K is treated as a fitting parameter, to be chosen such that all the curves collapse onto the same scaling curve [see Fig. 2]. When attempting to collapse the

$\Sigma(x)$ data, one faces two issues. First, the $\Sigma(x)$ data are non-monotonic in L , due to the fact that the sign of $\langle \vec{S}_i \cdot \vec{S}_j \rangle$ oscillates, and for curves scaled by different values of ξ_K , the oscillations are stretched by different amounts on a semilog plot. This introduces some “noise” to the $\Sigma(x)$ curves, making it somewhat difficult to decide when the scaling collapse is optimal. Second, for some parameter combinations, the condition $\xi_K \ll L$ is not met, and, therefore, perfect scaling cannot be expected for all the curves.

These issues can be dealt with by a two-step strategy: (i) we start with the curves, which collapse the best, namely, those with the smallest U/Γ ratios. These yield the smallest ξ_K values and hence satisfy the condition $\xi_K < L$ required for good scaling well enough such that the shape of the universal scaling curve can be established unambiguously (to the extent allowed by the aforementioned noise). (ii) We then proceed to larger ratios of U/Γ , which yield larger ξ_K , and adjust ξ_K such that a good collapse of $\Sigma(x)$ vs x/ξ_K onto the universal curve is achieved in the regime of small x/ξ_K , where finite-size effects are not yet felt. Thus, knowledge of the universal scaling curve allows ξ_K to be extracted even when the condition $\xi_K \ll L$ is not fully met.

The result of such a scaling analysis is shown in Fig. 2(a). A universal scaling curve can clearly be discerned, with deviations from scaling evident in the curves with large U/Γ , as expected. Moreover, Fig. 2(b) shows that the results for ξ_K extracted from $\Sigma(x)$ scaling agree rather well with the parameter dependence expected from Eq. (4) for $p/(\hbar v_F) \cdot \xi_K^0$ (with a prefactor of $p=6.8$), provided that $U/\Gamma \gtrsim 2$. For smaller U/Γ , no well-defined local moment will form and the premise for Eq. (4) no longer holds.

B. Scaling collapse of $\xi_a(L)$

A second strategy for extracting the screening length, following Refs. 6, 11, and 12, is to determine the length, say ξ_a , on which the integrated spin-correlation function $\Sigma(x)$ has dropped by a factor of a of its $x=0$ value (for instance, $a=0.9$ would signify a 90% screening of the local spin). Thus, we define

$$\xi_a(L) = \min\{x; \Sigma(x) \leq 1-a\}. \quad (5)$$

The argument of $\xi_a(L)$ serves as a reminder that this length depends on L , since the boundary condition $\Sigma(L-1)=0$ always enforces perfect screening for $x=L$. However, once the system size becomes sufficiently large ($L > \xi_K$) to accommodate the full screening cloud, $\xi_a(L)$ approaches a limiting value, to be denoted by ξ_a [shorthand for $\xi_a(\infty)$], which may be taken as a measure of the true screening length ξ_K . This is illustrated in the main panel of Fig. 1 for $a=0.9$: as L increases, the x values, where the $\Sigma(x)$ curves cross the threshold $1-a=0.1$ (horizontal dashed line), tend to a limiting value. This limiting value, reached in Fig. 1 for $L > 300$, defines $\xi_{0.9}$.

Figure 3 shows the L dependence of $\xi_{0.9}(L)$ for several values of U/Γ ranging from 0.4 to 12.5, and system sizes up to $L=500$. We observe that $\xi_{0.9}(L)$ reaches its limiting value for small ratios of U/Γ , which produce $\xi_{0.9}$ values smaller than $L=500$. For larger values of U/Γ , however, $\xi_{0.9}(L)$ does not saturate, implying that for these parameters, the true

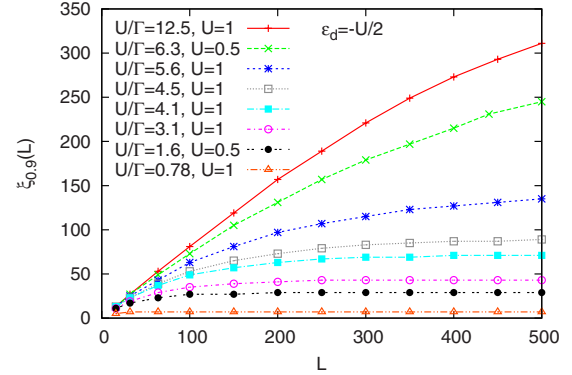


FIG. 3. (Color online) System size dependence of $\xi_{0.9}(L)$ for $\epsilon_d = -U/2$. Points represent numerical data; lines serve as guides to the eyes.

screening length is too large to fit into the finite system size.³⁶

Nevertheless, it is possible to extract the true screening length in the latter cases as well, by performing a two-step finite-size scaling analysis: (i) for those parameters U/Γ for which $\xi_a(L)$ has already saturated on a finite system, we set $\xi_a = \xi_a(L=500)$, and plot $\xi_a(L)/\xi_a$ vs L/ξ_a . This collapses all such curves onto a universal scaling curve. For larger U/Γ , we rescale the $\xi_a(L)$ curves in a similar fashion, but now using ξ_a as a fit parameter, chosen such that the rescaled curves collapse onto the universal curve determined in step (i). As shown in Fig. 4(a) for $a=0.9$, this strategy produces an excellent scaling collapse for all combinations of U and Γ studied here.

The above procedure requires the threshold parameter a to be fixed arbitrarily. Qualitatively, one needs a large a to capture most of the correlations, i.e., $\xi_a(L \rightarrow \infty) \sim \xi_K$, yet a ought not to be too close to one to avoid boundary effects in the results. Technically, the calculation of ξ_a is much easier the smaller a is, as less correlators $\langle \vec{S}_i \cdot \vec{S}_j \rangle$ that are of a small numerical value need to be computed to high accuracy (see also the discussion in the Appendix). For instance, at $U/\Gamma = 5$ and $L=500$, $\xi_{0.9} \approx 112$ sites, while $\xi_{0.75} \approx 29$ sites.

We have carefully analyzed the qualitative dependence of our analysis on the threshold a . First, the universal scaling behavior in $\xi_a(L)/\xi_a$ is seen for $a > 0.6$. Using too small a value for a ignores the long-range behavior of $\Sigma(x)$. Qualitatively, ξ_a needs to be close to the point, where the decay of the envelope of spin-spin correlations changes from a power law with $1/x$ to $1/x^2$ (see Fig. 2 in Ref. 13). Second, it turns out that different choices of a produce values of ξ_a that differ only by a (U -independent and Γ -independent) prefactor $p(a)$, as illustrated in Fig. 4(b) (symbols). In particular, for $U/\Gamma \gtrsim 2$, all ξ_a follow the same functional dependence on the parameters U and Γ , satisfying the relation

$$\xi_a = \frac{p(a)}{\hbar v_F} \xi_K^0 \quad (6)$$

expected from Eq. (4) (lines in Fig. 4). It is obvious that ξ_a yields an *upper* bound to ξ_K^0 since $p(a) > 1$ for all choices of a .

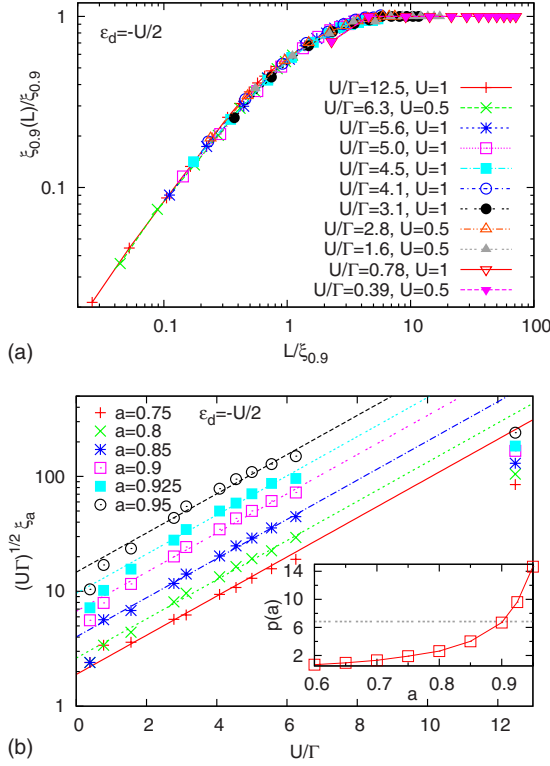


FIG. 4. (Color online) Results of a $\xi_a(L)$ scaling analysis for $\epsilon_d = -U/2$. (a) Scaling collapse of $\xi_{0,9}(L)/\xi_{0,9}$ vs $L/\xi_{0,9}$, obtained by the two-step scaling strategy described in the text in Sec. III B. (b) Comparison of the U and Γ dependence of ξ_a and ξ_a^0 [from Eq. (4)] for several values of a : $\sqrt{U\Gamma} \xi_a$ (symbols) and $\sqrt{U\Gamma} p(a) T_K^{-1}$ (lines) plotted vs U/Γ , using the fit parameters $p(a)$ shown in the inset plotted vs a . The dotted line in the inset indicates the prefactor $p = 6.8$ obtained from the $\Sigma(x)$ scaling analysis of Fig. 2(b).

The only exceptions are the data points at $U/\Gamma = 12.5$, for which ξ_a is too large in comparison to $L = 500$ to yield reliable results. The latter are thus excluded when fitting the ξ_a data to determine the best values for $p(a)$, shown in the inset of Fig. 4.

The inset includes the prefactor $p = 6.8$ (horizontal dotted line) obtained in Sec. III A, from Fig. 2, via a scaling analysis of $\Sigma(x)$ (which has the advantage of not involving any arbitrarily chosen threshold). Evidently, $p = 6.8$ is rather well matched by $p(0.9) \approx 6.7$, implying that the two alternative scaling strategies explored above, based on $\Sigma(x)$ and $\xi_a(L)$, yield essentially identical screening lengths for $a = 0.9$. For the remainder of this paper, where we consider $\epsilon_d \neq -U/2$ or $B \neq 0$, we shall thus determine the screening length by employing $\xi_{0,9}(L)$ scaling, which is somewhat more straightforward to implement than $\Sigma(x)$ scaling.

IV. GATE POTENTIAL

We next investigate the behavior of the Kondo screening length while sweeping the gate potential applied to the dot. Qualitatively, one expects the Kondo temperature to increase upon gating the dot away from particle-hole symmetry and eventually, as the dot's charge starts to deviate substantially

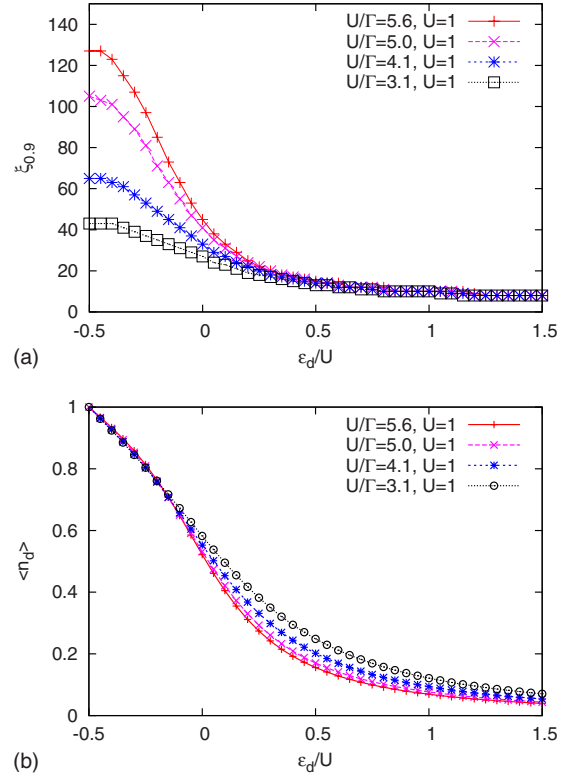


FIG. 5. (Color online) (a) Kondo screening length $\xi_{0,9}$ vs gate potential ϵ_d/U for several U/Γ and $L = 500$. (b) Dot occupation $\langle n_d \rangle$ vs gate potential.

from one, the Kondo effect will be fully suppressed.³⁷ Consequently, we expect the Kondo cloud to shrink upon varying ϵ_d . To elucidate this behavior, we focus on values of $U/\Gamma \lesssim 5.6$ for which $\xi_{0,9}(L = 500)$ yields a good estimate of the true ξ_K , as demonstrated in Sec. III.

Our results for $\xi_{0,9}$ are presented in Fig. 5(a). In addition, and as an illustration, we plot the dot level occupation $\langle n_d \rangle = \langle 0 | n_{d\uparrow} + n_{d\downarrow} | 0 \rangle$ in Fig. 5(b), where $|0\rangle$ is the ground state of the system, obtained via DMRG. As we shift the dot level away from the particle-hole symmetric point at $\epsilon_d = -U/2$ and thus leave the Kondo regime, $\xi_{0,9}$ falls off rapidly. This is symmetric in the direction of the deviation from the Kondo point. In the regime $\epsilon_d \lesssim -\Gamma$ one would expect Eq. (4) to hold roughly. Indeed, for $\epsilon_d = -U/4$, Eq. (4) still applies,³⁸ while for, e.g., $\epsilon_d = 0$ this is not the case anymore. The reason is that Eq. (4) is only valid in the Kondo regime with $\langle n_d \rangle \approx 1$. From Fig. 5(b) we see that the dot occupation starts to decrease quickly as we increase ϵ_d from $-U/2$, implying that the magnetic moment decreases as well. In the mixed-valence regime, $\epsilon_d \gtrsim -\Gamma$, $\xi_{0,9}$ measures the strength of the spin-spin correlations not originating from Kondo physics.

V. MAGNETIC FIELD

The application of a magnetic field is known to destroy the Kondo effect and its influence on the density of states (DOS) and the conductance has been widely studied.^{39,40} Here, we investigate how the screening cloud collapses as the magnetic moment is squeezed by the magnetic field. In

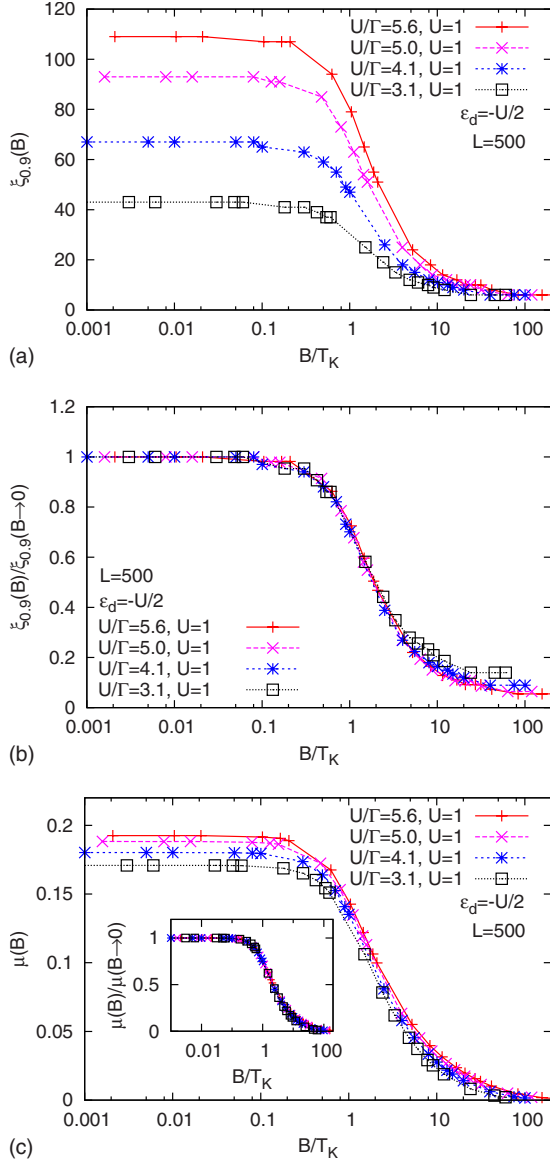


FIG. 6. (Color online) (a) Kondo screening length $\xi_{0,9}$ as a function of the magnetic field applied to the dot for $L=500$. In all panels, T_K is given by $T_K = \hbar v_F / \xi_K^0$ with ξ_K^0 from Eq. (4). (b) Scaling collapse of $\xi_{0,9}(B)/\xi_{0,9}(B \rightarrow 0)$ vs B/T_K (c) Magnetic moment $\mu = \langle (S_d^z)^2 \rangle - \langle S_d^z \rangle^2$ vs B/T_K . The inset shows the rescaled data $\mu(B)/\mu(B \rightarrow 0)$.

the presence of a finite magnetic field the total spin \vec{S} is no longer conserved but only S^z is conserved. Thus we are left with a $U(1)$ symmetry for S^z instead of the $SU(2)$ symmetry for \vec{S} . As a consequence, much more computational effort is needed in order to achieve an accuracy similar to the zero-field case (see the Appendix for detail).

Our results for (i) the screening length $\xi_{0,9}(L=500)$ and (ii) the magnetic moment of the dot $\mu = \langle (S_d^z)^2 \rangle - \langle S_d^z \rangle^2$ are displayed in Figs. 6(a) and 6(c), respectively. As the magnetic field is increased but still smaller than T_K , there are almost no visible effects in $\xi_{0,9}$ (note the logarithmic scale in the figure). Once the magnetic field B reaches the order of the Kondo temperature T_K , the Kondo effect gets suppressed and the extent of the Kondo cloud shrinks rapidly. More

precisely, a pronounced decay of the screening length sets in at $B \approx 0.5T_K$, in agreement with findings for the field-induced splitting of the central peak in the impurity spectral function.⁴¹ Qualitatively, both the screening length and the magnetic moment μ exhibit the same behavior. Note that for small U/Γ , charge fluctuations reduce the magnetic moment to lie below the value $\mu=1/4$ applicable for the Kondo model, which presupposes $U/\Gamma \gg 1$.

To identify the point at which the Kondo effect breaks down, we again study the collapse of results from Fig. 6 onto a universal curve. This is shown in Fig. 6(b), and as a main result we find

$$\frac{\xi_{0,9}(B)}{\xi_{0,9}(B \rightarrow 0)} \propto f(B/T_K), \quad (7)$$

where $f(x)$ describes the universal dependence on B/T_K . We note that due to higher numerical effort for calculations with a finite magnetic field (as further discussed in the Appendix) our numerical results slightly underestimate $\xi_{0,9}(B)$ at $U/\Gamma \gtrsim 5$, in particular, at small B . This, however, has no qualitative influence on the scaling collapse described by Eq. (7). We suggest that an analysis analogous to the one presented in Fig. 6 could be used to extract T_K for models in which the dependence of T_K on model parameters is not known. In such an analysis, T_K would be the only fitting parameter, since $\xi_{0,9}(B, L \rightarrow \infty)$ can be determined along the lines of Sec. III and one would obtain T_K up to an unknown prefactor, which is independent of U/Γ .

By rescaling the magnetic moment data to $\mu(B)/\mu(B \rightarrow 0)$ as shown in the inset of Fig. 6(c) we again find a universal curve very similar to the collapse of $\xi_{0,9}(B)/\xi_{0,9}(B \rightarrow 0)$ in Fig. 6(b). We thus confirm that a collapse of local quantities can be used to extract T_K , as previously shown using DMRG.⁸ In principle, both a scaling analysis of $\xi_{0,9}(B)$ and $\mu(B)$ can be used to extract T_K . Using the analysis of the screening length data (ξ_K) offers the possibility of a scaling analysis as outlined in Sec. III to reach parameter regimes, where a convergence of the data in L has not yet been reached. Moreover, the analysis of ξ_K directly unveils the relevant length scales.

VI. SUMMARY

In this work, we studied the spin-spin correlations in the single-impurity Anderson impurity model using a state-of-the-art implementation of the density matrix renormalization group method. We first considered the particle-hole symmetric point and discussed two ways of collapsing the system-size-dependent data onto universal scaling curves to extract a measure of the Kondo cloud's extension, the screening length ξ_K , as a function of U/Γ , or T_K , respectively. The first analysis is based on a scaling collapse of the integrated correlations, while the second one employs a finite-size scaling analysis of the distance $\xi_a(L)$ from the impurity at which a certain fraction a of the impurity's magnetic moment is screened. $\xi_a(L)/\xi_a(\infty)$ exhibits a universal dependence on $L/\xi_a(\infty)$, independently of the parameter U/Γ . We further showed that for an appropriately chosen value of the parameter a , both approaches yield quantitatively similar estimates

of the screening length. Our results for ξ_K , obtained from either of the scaling analyses, nicely follow the expected dependence on U/Γ .

As DMRG works in real space, the scaling regime could only be reached for $U/\Gamma=4$ and system sizes of $L \lesssim 500$, but even for larger $U/\Gamma \lesssim 6$, a collapse onto the universal behavior could be achieved. Note that $U/\Gamma \sim 4$ is the regime, in which time-dependent DMRG is able to capture Kondo correlations in real-time simulations of transport²⁷ on comparable system sizes, consistent with our observations.

While NRG is better suited to access the regime of very small Kondo temperatures T_K , DMRG efficiently gives access to the full correlation function $\langle \vec{S}_d \cdot \vec{S}_i \rangle$ in a single run. As an outlook onto future applications, we emphasize that DMRG allows for the calculation of the spin-spin correlations in the case of interacting leads¹² or out-of-equilibrium, which is challenging if not impossible for other numerical approaches with current numerical resources.

While the first part of our study focused on the particle-hole symmetric point where Kondo physics is dominant, we have further analyzed how the screening cloud is affected (i) by varying the gate voltage and tuning the system into the mixed-valence regime, and (ii) by applying a magnetic field at particle-hole symmetry. The latter provides an independent measure of the Kondo temperature, through the universal dependence of the screening length on T_K/B .

Note added: while finalizing this work, we became aware of a related effort on the Kondo cloud, Ref. 42, using the so-called embedded-cluster approximation, slave bosons, and NRG. Their analysis is based on calculating the local density of states in the leads, as a function of the distance from the impurity.

ACKNOWLEDGMENTS

We gratefully acknowledge fruitful discussions with E. Anda, L. Borda, C. Büsser, E. Dagotto, G. B. Martins, J. Riera, and E. Vernek. This work was supported by DFG (SFB 631, De-730/3-2, SFB-TR12, SPP 1285, and De-730/4-1). Financial support by the Excellence Cluster “Nanosystems Initiative Munich (NIM)” is gratefully acknowledged. J.v.D and F.H.M. thank the KITP at UCSB, where this work was completed, for its hospitality. This research was supported in part by the National Science Foundation under Grant No. NSF PHY05-51164.

APPENDIX: NUMERICAL DETAIL

In this Appendix we provide detail on our numerical method. The DMRG calculations presented in this work are challenging for two reasons. First, we model the conduction band with a chain of length L that provides an energy resolution of $1/L$, whereas the Kondo temperature becomes exponentially small with increasing U/Γ [c.f. Eq. (4)]. Second, the spin-spin correlators are long-ranged quantities making very accurate calculations of quantities necessary that are small compared to the unit of energy, t . The parameter controlling the accuracy of our calculations is the number of states m used to approximate the ground state during the

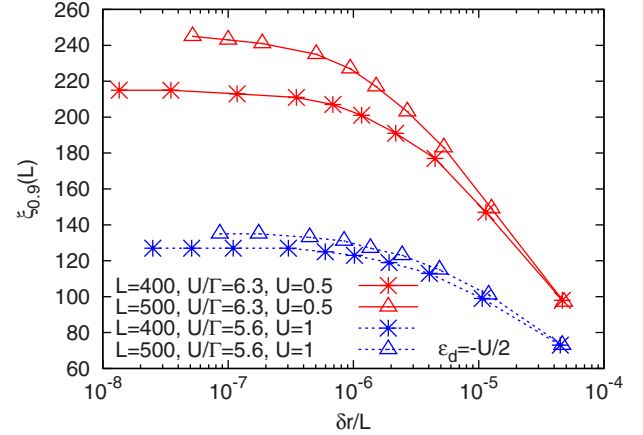


FIG. 7. (Color online) Convergence of $\xi_{0,9}$ vs the residual norm per site $\delta r/L$ for $\epsilon_d = -U/2$, extracted from ground-state calculations using the SU(2) symmetry. For each combination of U/Γ and L , the number of states kept increases for data points from right to left as $m=200, 400, 600, 800, 1000, 1200, 1500, 2000, 2500, 3000$, except for the case $U/\Gamma=5.6, L=500$, where no point with $m=3000$ is shown.

DMRG sweeps. Typically, we choose $m=1500$ (3000 at most) for the calculation of the ground state. This results in a residual norm per site,⁴³ a measure for the quality of the convergence of the calculated ground state toward an eigenstate of the Hamiltonian, $\delta r = \langle \psi_0 | (\hat{H} - E)^2 | \psi_0 \rangle$, on the order of $\frac{\delta r}{L} = \mathcal{O}(10^{-7})$.

Figure 7 illustrates the m dependence of $\xi_{0,9}$ for two values of U/Γ and two values of L at $\epsilon_d = -U/2$, obtained from simulations using the SU(2) symmetry. The larger the ratio U/Γ and the bigger the system size L , the higher the number of states m , needed to be kept to obtain a well-converged ground state, see Fig. 7. This can be understood as follows: higher U/Γ implies a smaller Kondo temperature, i.e., a

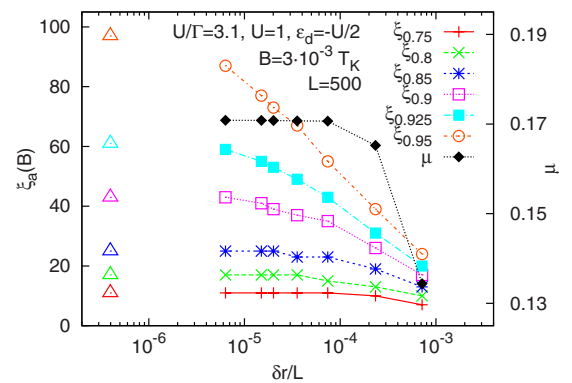


FIG. 8. (Color online) Convergence of $\xi_a(B)$ and the magnetic moment μ vs the residual norm per site $\delta r/L$ for a finite magnetic field of $B/T_K = 3 \cdot 10^{-3}$ and $\epsilon_d = -U/2$. For comparison, we add the $B=0$ data, represented by the open triangles, from calculations exploiting the SU(2) symmetry ($m=1500$ states kept). The calculation with a magnetic field (symbols connected with lines) uses the U(1) symmetry only ($m=100, 200, 400, 600, 800, 1000, 1500$ states kept from right to left). The results for the dot's magnetic moment μ are also included for comparison (solid diamonds).

larger screening length $\xi_{0,9}$ and longer-ranged spin-spin correlators $\langle \vec{S}_d \cdot \vec{S}_i \rangle$. A well-converged ground state requires these to be evaluated accurately over the entire range $i \leq \xi_{0,9}$, and hence more states need to be kept during the DMRG sweeps. For the scaling analysis presented in Sec. III (see Figs. 2 and 4), we only used data points that are converged with respect to the number of states kept.

In Fig. 8, we illustrate that the convergence with the number of states is greatly accelerated whenever the SU(2) symmetry can be exploited. We compare this preferable case to the calculations with a magnetic field, where the SU(2) symmetry is reduced to a U(1) symmetry. In the figure, we use a small magnetic field of $B/T_K = 3 \cdot 10^{-3}$, such that the results for $\xi_a(B, L=500)$ coincide with the results for $B=0$, previously obtained from the SU(2) calculation. For instance, at $L=500$ by keeping $m=1500$ states, $\delta r \approx 3 \cdot 10^{-3}$ is reached in

the U(1) case as compared to $\delta r \approx 2 \cdot 10^{-4}$ for the SU(2) case. For $U=1$, $\Gamma=0.32$, we show that this residual norm ensures accurate data for ξ_a up to $a=0.9$, while for larger a , our U(1) results are well below the corresponding SU(2) ones computed with the same m .

Pragmatically, in the case of broken SU(2) symmetry, one may resort to using a smaller threshold a (instead of $a=0.9$), for which the convergence with m is faster. As we have shown in Fig. 4, ξ_K can be extracted from ξ_a with $0.6 \leq a \leq 0.95$ up to a nonuniversal prefactor using the schemes discussed in Sec. III.

In contrast to the screening length, the calculation of the magnetic moment μ , a local quantity, is much better behaved. Thus μ does not suffer much from the slower convergence of the U(1) calculation and converges quickly to a high precision (displayed as diamonds in Fig. 8).

-
- ¹J. Kondo, Prog. Theor. Phys. **32**, 37 (1964).
²W. G. van der Wiel, S. De Franceschi, J. M. Elzerman, T. Fujisawa, S. Tarucha, and L. P. Kouwenhoven, Rev. Mod. Phys. **75**, 1 (2002).
³D. Goldhaber-Gordon, H. Shtrikman, D. Mahalu, D. Abusch-Magder, U. Meirav, and M. A. Kastner, Nature (London) **391**, 156 (1998).
⁴W. Liang, M. P. Shores, M. Bockrath, J. R. Long, and H. Park, Nature (London) **417**, 725 (2002).
⁵B. Zheng, C. Lu, G. Gu, A. Makarovski, G. Finkelstein, and J. Liu, Nano Lett. **2**, 895 (2002).
⁶J. E. Gubernatis, J. E. Hirsch, and D. J. Scalapino, Phys. Rev. B **35**, 8478 (1987).
⁷V. Barzykin and I. Affleck, Phys. Rev. Lett. **76**, 4959 (1996).
⁸E. S. Sørensen and I. Affleck, Phys. Rev. B **53**, 9153 (1996).
⁹I. Affleck and P. Simon, Phys. Rev. Lett. **86**, 2854 (2001).
¹⁰E. S. Sørensen and I. Affleck, Phys. Rev. Lett. **94**, 086601 (2005).
¹¹T. Hand, J. Kroha, and H. Monien, Phys. Rev. Lett. **97**, 136604 (2006).
¹²S. Costamagna, C. J. Gazza, M. E. Torio, and J. A. Riera, Phys. Rev. B **74**, 195103 (2006).
¹³L. Borda, Phys. Rev. B **75**, 041307(R) (2007).
¹⁴I. Affleck, L. Borda, and H. Saleur, Phys. Rev. B **77**, 180404(R) (2008).
¹⁵R. G. Pereira, N. Laflorencie, I. Affleck, and B. I. Halperin, Phys. Rev. B **77**, 125327 (2008).
¹⁶P. Simon and I. Affleck, Phys. Rev. B **68**, 115304 (2003).
¹⁷W. B. Thimm, J. Kroha, and J. von Delft, Phys. Rev. Lett. **82**, 2143 (1999).
¹⁸V. Madhavan, W. Chen, T. Jamneala, M. F. Crommie, and N. S. Wingreen, Science **280**, 567 (1998).
¹⁹H. C. Manoharan, C. P. Lutz, and D. M. Eigler, Nature (London) **403**, 512 (2000).
²⁰S. R. White, Phys. Rev. Lett. **69**, 2863 (1992).
²¹S. R. White, Phys. Rev. B **48**, 10345 (1993).
²²U. Schollwöck, Rev. Mod. Phys. **77**, 259 (2005).
²³K. G. Wilson, Rev. Mod. Phys. **47**, 773 (1975).
²⁴R. Bulla, T. A. Costi, and T. Pruschke, Rev. Mod. Phys. **80**, 395 (2008).
²⁵L. Borda, M. Garst, and J. Kroha, Phys. Rev. B **79**, 100408(R) (2009).
²⁶K. Chen, C. Jayaprakash, and H. R. Krishnamurthy, Phys. Rev. B **45**, 5368 (1992).
²⁷K. A. Al-Hassanieh, A. E. Feiguin, J. A. Riera, C. A. Büsser, and E. Dagotto, Phys. Rev. B **73**, 195304 (2006).
²⁸S. Kirino, T. Fujii, J. Zhao, and K. Ueda, J. Phys. Soc. Jpn. **77**, 084704 (2008).
²⁹F. Heidrich-Meisner, A. E. Feiguin, and E. Dagotto, Phys. Rev. B **79**, 235336 (2009).
³⁰While we use a matrix-product-states-based implementation of DMRG,³² for the problem studied here, equivalently good results can be obtained with standard DMRG codes that exploit sufficiently many good quantum numbers.
³¹I. P. McCulloch and M. Gulácsi, EPL **57**, 852 (2002).
³²I. P. McCulloch, J. Stat. Mech. (2007), P10014.
³³F. Heidrich-Meisner, G. B. Martins, C. A. Büsser, K. A. Al-Hassanieh, A. E. Feiguin, G. Chiappe, E. V. Anda, and E. Dagotto, Eur. Phys. J. B **67**, 527 (2009).
³⁴F. D. M. Haldane, J. Phys. C **11**, 5015 (1978).
³⁵R. Zitko, J. Bonca, A. Ramsak, and T. Rejec, Phys. Rev. B **73**, 153307 (2006).
³⁶We note that by definition $\xi_a(L)$ is only accurate up to one lattice constant. As a consequence, very small changes in $\langle \vec{S}_d \cdot \vec{S}_i \rangle$ may cause a change in $\xi_a(L)$ by one. This can be seen in, e.g., the data for $U=1$, $\Gamma=0.22$ from Fig. 3 (open squares), where $\xi_{0,9}(L)$ is very close to convergence in L but still increases between $L=450$ and $L=500$ by one.
³⁷A. C. Hewson, *The Kondo Problem to Heavy Fermions* (Cambridge University, Cambridge, England, 1997).
³⁸Note that the prefactor p depends on the gate potential, i.e., $p = p(\epsilon_d)$.
³⁹T. A. Costi, Phys. Rev. B **64**, 241310(R) (2001).
⁴⁰A. Rosch, T. A. Costi, J. Paaske, and P. Wölfle, Phys. Rev. B **68**, 014430 (2003).
⁴¹T. A. Costi, Phys. Rev. Lett. **85**, 1504 (2000).
⁴²C. A. Büsser, G. B. Martins, L. C. Ribeiro, E. Vernek, E. V. Anda, and E. Dagotto, arXiv:0906.2951 (unpublished).
⁴³A. Weichselbaum, F. Verstraete, U. Schollwöck, J. I. Cirac, and J. von Delft, Phys. Rev. B **80**, 165117 (2009).